ADVANCED FUNCTIONAL MATERIALS
www.afm-journal.de

Tailored Mechanical Metamaterials with Programmable Quasi-Zero-Stiffness Features for Full-Band Vibration Isolation

*Quan Zhang, Dengke Guo, and Gengkai Hu**

Quasi-zero-stiffness (QZS) isolators of high-static-low-dynamic stiffness play an important role in ultra-low frequency vibration mitigation. While the current designs of QZS mainly exploit the combination of negative-stiffness corrector and positive-stiffness element, and only have a single QZS working range, here a class of tailored mechanical metamaterials with programmable QZS features is proposed. These programmed structures contain curved beams with geometries that are specifically designed to enable the prescribed QZS characteristics. When these metamaterials are compressed, the curved beams reach the prescribed QZS working range in sequence, thus enabling tailored stair-stepping force-displacement curves with multiple QZS working ranges. Compression tests demonstrate that a vast design space is achieved to program the QZS features of the metamaterials. Further vibration tests confirm the ultra-low frequency vibration isolation capability of the proposed mechanical metamaterials. The mechanism of QZS stems solely from the structural geometry of the curved beams and is therefore materials-independent. This design strategy opens a new avenue for innovating compact and scalable QZS isolators with multiple working ranges.

1. Introduction

Isolation of undesirable vibrations is required for many engineering structures and precision equipment.[1] From a passive perspective, vibrations can be isolated through inserting an isolator between the vibration source and the system to be protected. Theoretically, the performance of any isolator can be improved by lowering its natural frequency; the softer the isolator, the lower the natural frequency, and the better the performance of the isolator. However, it is unrealistic to make the stiffness of an isolator ultra-small (even to zero) because it will collapse under the own load of the object to be isolated. Therefore, ultra-low frequency isolation performance could not be possible to be achieved by using traditional passive linear and/or nonlinear vibration isolators.

To overcome this limitation, customized nonlinear springs have been used to obtain a high static stiffness and hence a sufficient loading capacity, and a low dynamic stiffness which results in a low natural frequency. The so-called quasi-zero-stiffness (QZS)[2,3] isolators of high-static-low-dynamic stiffness are found to have nearly zero overall dynamic stiffness without sacrificing the loading capacity, showing promising application prospects in ultra-low frequency vibration isolation.[4] Mechanically speaking, a plateau will be observed on the force–displacement curve of the QZS isolator, indicating that the force is nearly constant within a small displacement range, that is, the tangent stiffness is zero. When the isolator is loaded with a suitable sized mass, exactly making the isolator compressed to arrive at the plateau, the dynamic stiffness of the isolator becomes zero. Here, the force corresponding to the plateau is named as QZS payload. Currently, the vast majority of QZS isolators are generally achieved by connecting a negative stiffness element (usually realized through oblique springs,[5,6] buckled beams,[7,8] magnet rings,[9] etc.) with a positive stiffness element in parallel, which makes the isolator complicated, and not compact enough to implement applications in small scale. Moreover, QZS isolators based on these mechanisms generally have a single preferred working position where the positive stiffness is substantially neutralized by the negative stiffness. Thus, the working range (the displacement range of the plateau on the force–displacement curve) of such QZS isolator is very narrow, and the mass of the object to be isolated (i.e., the QZS payload) is uniquely determined, to ensure that the isolator arrives at its working position under the action of this mass.

Aiming at solving these problems, we explore the design idea from compliant mechanism,[10] which realizes its function by harnessing deformation of flexible elastic elements. More recently, of particular interest in this research field is designing compliant metamaterials to achieve programmable features of shape reconfiguration,[11–14] mechanical stiffness,[15–20]

Dr. Q. Zhang, Dr. D. K. Guo, Prof. G. K. Hu
Key Laboratory of Dynamics and Control of Flight Vehicle, Ministry of Education, School of Aerospace Engineering
Beijing Institute of Technology
Beijing 100081, China
E-mail: hugeng@bit.edu.cn

The ORCID identification number(s) for the author(s) of this article can be found under https://doi.org/10.1002/adfm.202101428.

DOI: 10.1002/adfm.202101428

information encryption,[21–24] energy absorbing,[25–28] wave guiding,[29–32] bandgap,[33–35] solitons,[36] etc., motivating possible way for novel QZS isolator. Here, we suggest and realize a class of tailored mechanical metamaterials containing many optimally designed curved beams; these beams are tailored in shape to achieve prescribed QZS characteristics, enabling the whole mechanical metamaterial to achieve programmable QZS features. The main innovations of this work lie in the following two aspects: i) The achieved QZS is originated from the tailored mechanical geometrical nonlinearities of monolithic compliant mechanism (here refers to the optimally designed curved beam) directly,[37–39] rather than counteracting the positive stiffness of an elastic element by another negative stiffness element, thus significantly reducing the complexity to achieve a QZS isolator. ii) More importantly, by assembling the unit cell of the mechanical metamaterials, a basic building block that contains two identical tailored curved beams, programmable QZS features including both the QZS displacement range and the QZS payload can be achieved. This programming strategy has not been reported by previous works related to achieving QZS,[37–39] which report only a single QZS region. To emphasize these aspects, proof-of-principle experiments on 3D printed architectures are presented.

2. Results and Discussion

The core idea for constructing the tailored mechanical metamaterials with programmable QZS features is illustrated in **Figure 1**. Consider a force-displacement curve with a plateau, which means that the reaction force remains unchanged as the displacement along with that direction increases in a certain

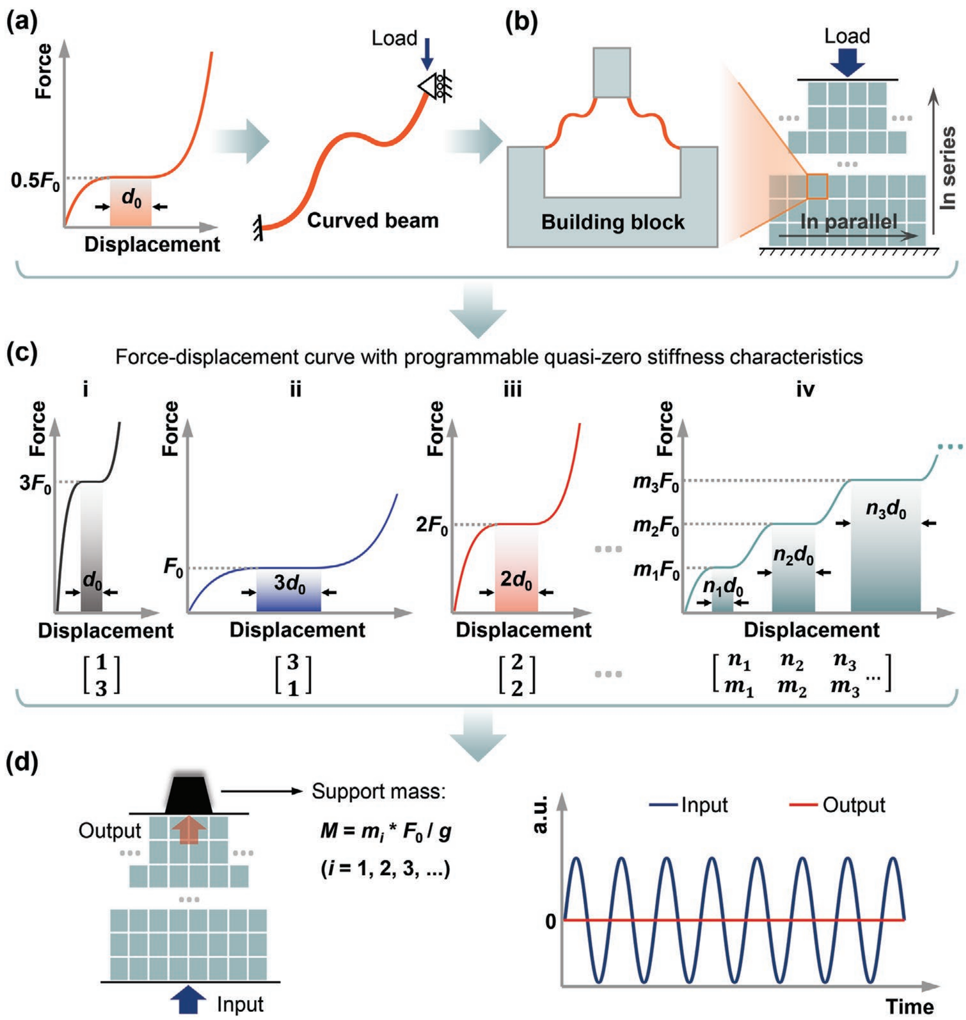

Figure 1. Schematic diagram of the design of mechanical metamaterials with programmable QZS features. a) Assume a curved beam is compressed vertically at the top end while constraining the motion of both ends in the horizontal direction, its geometry is tailored to achieve a force–displacement relation with the prescribed QZS feature (corresponding to the plateau, which means that the reaction force remains unchanged at $0.5{*}F_0$ over the displacement range d_0). b) To construct a basic building block, two identical curved beams are arranged symmetrically and connected by stiff horizontal strips. When the building block is compressed vertically at the top, the boundary condition of an individual beam is the same as that illustrated in (a). c) Force–displacement relation with programmable QZS characteristics can be achieved by the mechanical metamaterial assembled from the building block. d) When the mass of an object corresponds to the force at the plateau on the force-displacement curve of the mechanical metamaterial, it will be isolated from vibration nearly over the full band.

loading range. Our priority is to find the geometry of a curved beam, whose loading response curve exactly matches the desired "plateau" characteristics (the load remains unchanged at $0.5*F_0$ over the displacement range d_0, i.e., the expected QZS characteristics), as illustrated in Figure 1a. Further, to construct a practically useful building block (unit cell of mechanical metamaterial) out of individual curved beams, two additional conditions need to be fulfilled. i) Asymmetric deformation of the building block must be prevented because the slip boundary condition is adopted for the individual curved beams (see Figure 1a). ii) Lateral motion of the ends of the individual curved beams must be constrained. In the blueprint unit cell shown in Figure 1b, these two aspects are accomplished; two identical curved beams are arranged symmetrically and connected by stiff horizontal strips (a similar arrangement also see refs. [25, 40, 41], which aim at realizing multistable mechanical metamaterials for elastic energy trapping). Because the two curved beams are arranged in parallel in the building block, its QZS payload is doubled to F_0.

By assembling the identical building blocks in series and parallel (see Figure 1b), a programmable QZS behavior can be achieved, as illustrated in Figure 1c. The mechanism can be interpreted by the analog of connecting Hooke's springs in parallel and series.[26] For the case of connecting in parallel, the deformations on all individual elements equal to the external deformation, and the individual forces add up to the total force. For instance, by assembling three building blocks in parallel, we arrive at a plateau quantified by matrix "[1; 3]" (see Figure 1c(i)), where the first number represents the resulting QZS displacement range normalized by d_0, and the second number represents the resulting QZS payload normalized by F_0. For the case of connecting in series, the forces on all individual elements equal to the external force, and the individual deformations add up to the total deformation. Correspondingly, three building blocks connected in series will lead to a QZS behavior quantified by matrix "[3; 1]" (see Figure 1c(ii)). The combination of these two rules generates rich QZS features, even a stair-stepping force–displacement curve with multiple plateaus, as illustrated in Figure 1c(iii,iv), which are quite different from previous studies[11,26] combining numbers of bistable units in series. As mentioned in Section 1, the achieved programmable QZS can be used to isolate ultralow frequency vibrations without sacrificing the loading capacity. When the mass of the object needs to be isolated from vibration equals to m_i*F_0/g (g is the gravitational acceleration), which corresponds to a plateau on the force-displacement curve (Figure 1c(iv)), dynamic input disturbance will be isolated nearly over the full band (Figure 1d). Therefore, compared to traditional QZS isolators with only a single QZS region, the mechanical metamaterial maintains its excellent vibration isolation performance under different support masses because there are multiple plateaus on the force–displacement curve.

To thoroughly demonstrate this strategy, we start with designing the shape of curved beam for prescribed quasi-zero stiffness. As shown in **Figure 2**a, a curved beam is deformed by applying a vertical displacement to the top end, while constraining the motion of both ends in the horizontal direction. The curved beam is enclosed in a rectangular design space of sides L and H. Its shape can be defined by a non-uniform rational B-spline (NURBS[42]) with six control points (P_1–P_6) (see Supporting Information for details). The positions of P_1 and P_6 (coincide with the ends of the curved beam) are fixed in the corner of the design space, while the positions of P_2–P_5 are design variables.

The design objective is that the reaction force remains unchanged in a certain displacement range. For this reason, eight target points (see Figure 2b) are chosen to define the desired QZS feature. The choice of the number of target points is discussed in Supporting Information. Thus, the objective becomes minimizing the error between the actual force from the curved beam and the desired constant force at these eight points. Combining with proper constraints on design variables, the complete mathematical formula of this geometry optimization can be built (see details in Supporting Information). This optimization is performed based on the well-known genetic algorithm (GA). During the optimization process, the deformation of the curved beam is calculated by using the Beam Interface (Timoshenko formulation is adopted) in the commercial software COMSOL Multiphysics. The curved beam is meshed to about 90 beam elements, and MUMPS is selected as the solver to obtain the geometric nonlinear responses. The simulation convergence is testified by refining the mesh and obtaining the corresponding results (see Supporting Information for details). E is the Young's modulus and ν the Poisson's ratio of the constituent material. Throughout this paper, we use $E = 1.4$ GPa and $\nu = 0.4$, corresponding to a typical photosensitive resin material amenable to 3D additive manufacturing. The out-of-plane thickness of the curved beam is $d = 10$ mm. Considering the manufacturing accuracy of 3D printing, the in-plane thickness of the curved beam is chosen to be $t = 1$ mm. The other known parameters include i) side lengths of the design space $L = 30$ mm and $H = 15$ mm, and ii) endpoint coordinates of the beam $P_1 = [0, 0]$ and $P_6 = [L, H]$. Giving the knot vector and polynomial degree of the NURBS (see Supporting Information), the remaining design variables are i) the coordinates of $P_2 - P_5$, i.e., $[P_{ix}, P_{iy}]$ ($i = 2, 3, 4, 5$), and ii) weights of the NURBS basis functions, that is, w_j ($j = 1, 2, 3, 4, 5, 6$).

Following the above optimization procedure, for the desired QZS feature, that is, the reaction force stays constant at 2 N for these eight targeted loading points (Figure 2b, see Supporting Information for specific displacement values), we obtain a curved beam with the geometry parameters: $P_2 = [0.0744\ L, 0.3389\ H]$, $P_3 = [0.4113\ L, 0.2393\ H]$, $P_4 = [0.6306\ L, 0.5506\ H]$, $P_5 = [0.9719\ L, 0.2703\ H]$, $w_1 = 1.5794$, $w_2 = 2.3799$, $w_3 = 1.7017$, $w_4 = 3.0865$, $w_5 = 3.9529$, $w_6 = 3.3716$. The force–displacement curve of the obtained NURBS beam is shown by the red solid line in Figure 2b, which resembles a QZS behavior by approaching the prescribed target values. It should be noted that this curve is very probably not optimal globally, considering that the genetic algorithm generally outputs the local optimal solution. The optimization results by using more or fewer control points are also presented in Figure S5, Supporting Information. It seems that increasing the number of control points does not necessarily lead to a more optimal curve without changing the population size and termination generation. Besides, increasing the number of control points means increasing the number of optimization variables, which finally increases the cost of optimization design. To validate the effectiveness of the design, we build the corresponding 3D solid model and investigate its response under the boundary condition depicted in Figure 2a by using the commercial finite element

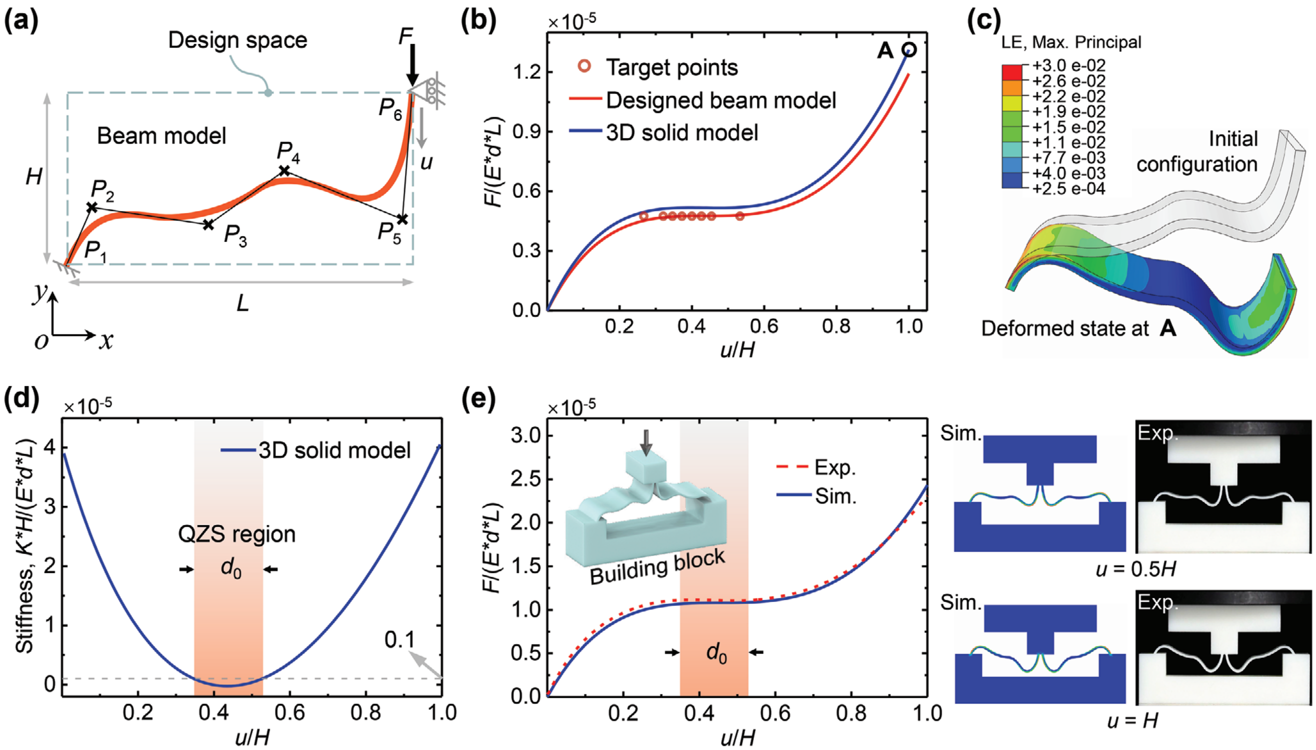

Figure 2. Mechanical behavior of the tailored curved beam, and the corresponding basic building block. a) Geometric representation and design boundary of the curved beam. b) Eight target points in the force-displacement space are chosen to define the expected QZS behavior. By using the geometry optimization method, the shape of the curved beam enclosed in the design space shown in (a) can be obtained, whose force–displacement curve (red) fits these target points very well. For comparison, the mechanical response of the corresponding 3D solid model is also presented (blue), which also exhibits the desired QZS feature. c) The distribution of the maximum principal strain for the loading displacement $u = H$. d) The stiffness is derived from the blue curve in (b). A QZS region is defined by selecting the normalized stiffness with a value of 0.1 as a threshold. e) Left panel: loading response of the basic building block under vertical compression. The simulated and experimental results are shown in blue and red, respectively. Right panel: the deformed configurations at loading states $u = 0.5H$ and $u = H$.

package ABAQUS. For details about the simulations, including the verification of convergence, see Supporting Information. The force–displacement relation of this solid model (the blue line in Figure 2b) also exhibits the desired QZS feature, although the position of the plateau corresponding to the QZS moves up slightly. The reason for the difference is that the out-of-plane thickness of the beam is relatively large, which is equivalent to the plane strain problem, while the Beam Interface simulation in COMSOL is closer to the plane stress problem. Figure 2c illustrates the deformed shape of the solid model for the loading displacement $u = H$, with the color map representing the maximum principal strain. The strains are less than 3% such that using a linear elastic constitutive relation in the simulations for simplicity is feasible.[19] The maximum principal strain can be further reduced by decreasing the in-plane thickness of the beam (see Figure S6, Supporting Information). Furthermore, the stiffness is depicted in Figure 2d, which is derived from the blue curve in Figure 2b. It is observed that the normalized stiffness decreases from about 4 to 0 and then increases back to 4, forming a QZS region. Quantitatively, normalized stiffness with a value of 0.1 is selected as a threshold to define the QZS region, as illustrated in Figure 2d. Altogether, we have obtained a monolithic smooth curved beam with the prescribed QZS feature.

To form a mechanical metamaterial with programmable QZS characteristics, a basic building block, as depicted by the inserted figure in Figure 2e, is constructed in the manner shown in Figure 1b. Its response under vertical displacement loaded on the top is investigated in ABAQUS, and the corresponding force–displacement relation is given by the blue line in Figure 2e. In the previously defined QZS region, the reaction force almost keeps constant. Compared with the blue curve in Figure 2b, one can see that the QZS payload (force corresponding to the plateau) is doubled due to the superposition effect of two parallel beams. Meanwhile, a building block sample is fabricated by using 3D additive manufacturing (SPS450H, National Institute Corporation of Additive Manufacturing, Xi'an, China) with a photosensitive resin (6000B, The Zhbond Company, China; $E = 1.4$ GPa and $\nu = 0.4$). The corresponding experimentally measured loading response is presented by the red dotted line, which also shows obvious QZS characteristics. Besides, the deformed configurations of the building block at the loading states $u = 0.5H$ and $u = H$ are reported in the right panel of Figure 2e, indicating that our experimental and numerical results are in good agreement.

When compressing the metamaterial formed from assembling the basic building block in series and parallel, its QZS feature can be predicted by the digitalization of the metamaterial. Taking the metamaterial consisting of N layers as an example (as illustrated in **Figure 3**a), and these layers are grouped according to the number of cells (i.e., the building blocks)

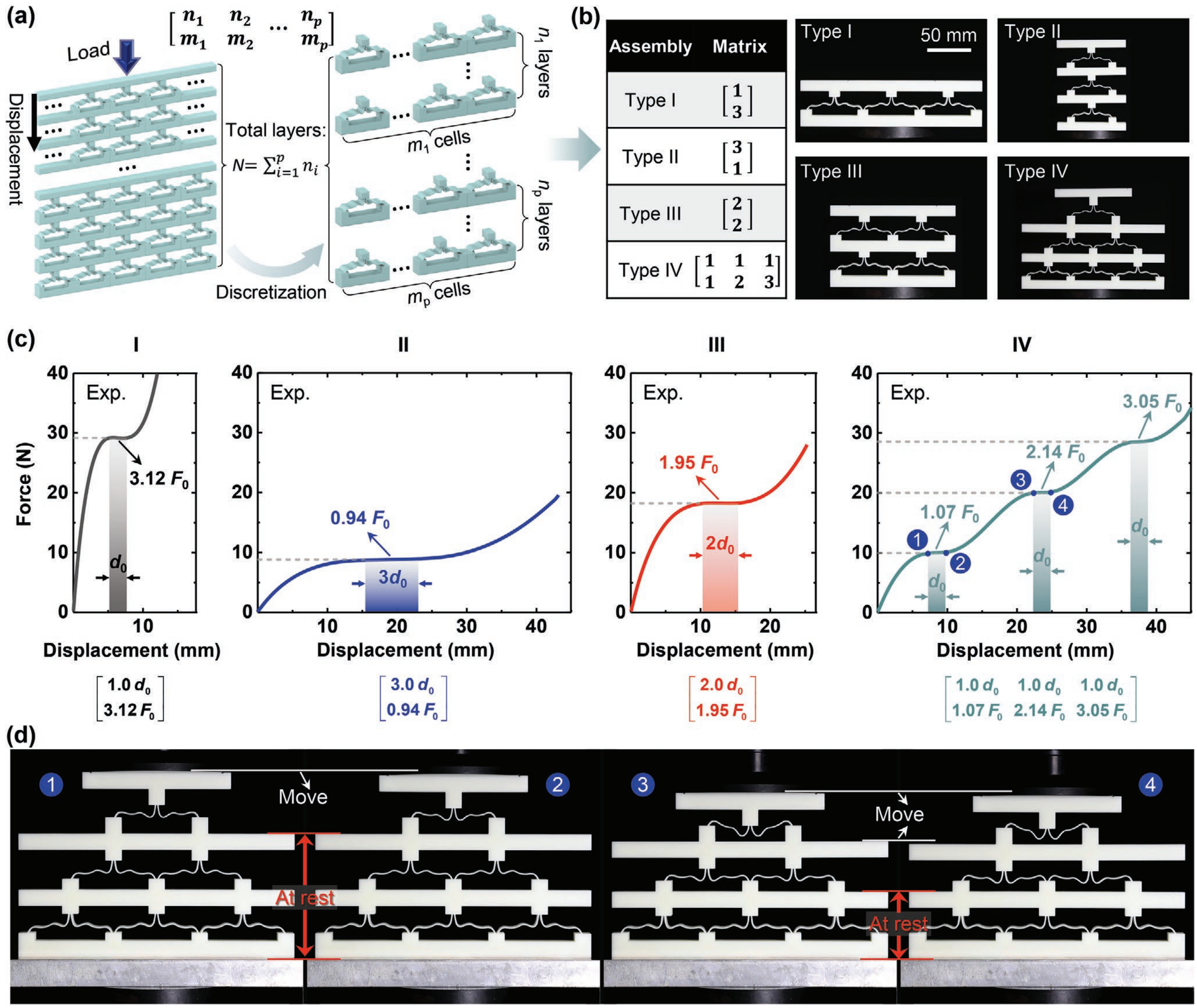

Figure 3. Programmable mechanical behavior of the tailored metamaterial. a) Digitalization of the assembly relation of the metamaterial. The layers of the metamaterial are grouped according to the number of cells therein. Supposing the i-th group is composed of n_i (i = 1, 2, ..., p) layers, with each layer containing m_i cells. b) Four metamaterial samples, respectively labeled as type I, type II, type III, and type IV, are fabricated by using 3D additive manufacturing. The assembly matrixes of them are illustrated in the left panel. c) The experimentally measured compression responses of these four metamaterial samples. The width and height of each QZS region are respectively measured by d_0 = 2.5 mm and F_0 = 9.36 N, which are obtained from the force-displacement response of the single cell shown in Figure 2e. d) Four typical deformation states during the loading process of the assembly type IV. The positions of these four states are marked in c(IV).

therein. Assuming there are p groups, and the i-th group is composed of n_i (i = 1, 2, ..., p) layers, with each layer containing m_i cells, we have $N = \sum_{i=1}^{p} n_i$. In this manner, the assembly relation of the metamaterial can be digitalized by the matrix [n_1 n_2 ... n_p; m_1 m_2 ... m_p] (see Figure 3a). Because all layers are in series, the total resultant force in each layer is the same. This indicates that the more cells the layer has, the smaller the resultant force in a single cell is, and the later the layer arrives at the QZS plateau. Therefore, according to the number of cells in each layer, the p groups will arrive at their QZS plateaus in sequence, that is, p plateaus will be observed on the force-displacement curve of the metamaterial. For the i-th plateau, corresponding to the i-th group, the QZS displacement range is superposed to be $n_i{*}d_0$ since the i-th group contains n_i layers in series, and the QZS payload is superposed to be $m_i{*}F_0$ since each layer in the i-th group contains m_i cells in parallel. d_0 and F_0, respectively, represent the QZS displacement range and the QZS payload of the single cell. Consequently, the QZS behavior of the metamaterial can be expressed as the $2 \times p$ matrix [$n_1{*}d_0$ $n_2{*}d_0$ ... $n_p{*}d_0$; $m_1{*}F_0$ $m_2{*}F_0$ ... $m_p{*}F_0$], with each column of the matrix corresponding to a plateau on the force-displacement curve (see Figure 1c).

To validate the predicted QZS features of the tailored metamaterial, four metamaterial samples, respectively, labeled as type I, type II, type III, and type IV (see Figure 3b), are fabricated by using 3D additive manufacturing mentioned above. For all the printed samples throughout this paper, the out-of-plane thickness is 20 mm. According to the digitalization scheme in Figure 3a, each assembly type can be digitally expressed by a matrix, as presented in the left panel of Figure 3b. For instance, the assembly type I contains only one layer with three cells in parallel, thus it corresponds to the matrix [1; 3]. Then the mechanical responses of these four samples are tested by utilizing an MTS testing machine (WDW-2, Changchun New Testing Machine Co., LTD, China) with a compressing speed of 10 mm min^{-1}, and the loading force is measured by a force sensor with a resolution of 0.01 N. The corresponding loading curves are shown in Figure 3c. These measured curves exhibit diverse QZS characteristics, specifically in the QZS displacement range and the QZS payload. For quantitative comparison, the QZS regions on each curve are highlighted by the columnar strips. The width and height of the QZS region are respectively measured by $d_0 = 2.5$ mm and $F_0 = 9.36$ N, which are obtained from the force–displacement response of a single cell (see Figure 2e). For each case, the measured QZS feature shows good agreement with the predicted one. Taking the assembly type I as an example, the measured QZS characteristics is denoted as [1.0*d_0; 3.12*F_0], which is very close to the predicted matrix [1.0*d_0; 3.0*F_0].

Furthermore, four typical deformation states during the loading process of the assembly type IV are presented in Figure 3d. The positions of these four states are marked in Figure 3c(IV). Among them, the first two respectively correspond to the start and end of the first QZS plateau, and the last two respectively correspond to the start and end of the second QZS plateau. According to the analysis in the previous paragraph, the three plateaus in Figure 3c(IV) correspond to the deformations of the first, second, and third layers, respectively. During each plateau, except for the layer corresponding to the plateau, no deformation occurs in the other layers because they do not "feel" the change of resultant force. This is responsible for the phenomenon observed in Figure 3d, that is, some stiff horizontal strips are at rest.

In addition to the above loading responses, we also recorded the full loading and unloading force–displacement curves for the printed unit cell and the type II metamaterial (see Figure S7, Supporting Information). The cycle responses show that the designed metamaterial almost returns to the initial shape when fully unloaded. The recovery rate of deformation reaches about 92.7%, which is obtained by comparing the residual displacement with total applied displacement. The cycle responses also illustrate that the unloading curve does not coincide with the loading curve, which is related to the inevitable energy dissipation of the polymeric material during the loading/unloading cycle. Be noted that, the QZS feature during the second cycle almost remains the same as that during the first cycle despite the existence of energy dissipation. Such energy dissipation could be reduced significantly if using metal as the constitutive material to fabricate the designed metamaterials.

There are several points that need to be briefly discussed as follows: First, according to the analysis in Figures 1 and 3, ideally, as for the mechanical metamaterial consisted of curved beams with identical geometry, its QZS payloads can only be a positive integer multiple of F_0. Naturally, such a question will be considered, that is, how to generate other QZS payloads that are not integral multiples of F_0? This issue can be addressed by introducing curved beams with different QZS characteristics, as demonstrated by Figure S8, Supporting Information. Second, the constitutive material used in the design is considered to be linearly elastic, the mechanism of QZS stems solely from the structural geometry of the curved beams and is therefore materials-independent. For example, when the constitutive material is changed from the photosensitive resin to aluminum, the normalized force–displacement curve remains almost unchanged (see Figure S9, Supporting Information). Third, the design strategy can be applied to structures with various length scales (from micro to macro). To demonstrate it, we proportionately reduce the geometric dimension of the designed curved beam (Figure 2a) by 1000 times and calculate the corresponding compressing responses. As shown by Figure S10, Supporting Information, when the length of the structure is changed from millimeter-scale to micron scale, the QZS characteristics are maintained although the magnitude of the loading force changed dramatically (decreased by six orders of magnitude). It should be noted that the size effect which can make the properties of the constitutive material greatly change is not considered here. Fourth, the programmability of the metamaterials originates from assembling the unit cells in series and parallel. In the current study, the arrangement of the unit cells is indeed in the two-dimensional plane. In practical application, we can arrange the unit cells along the direction normal to the plane of the paper; an example design is given by Figure S11, Supporting Information. Last, recent studies[43,44] also reported the plateau feature on the stress-strain curves of composite lattice metamaterials. These stress plateaus originate from buckling and post yielding of the microstructure. However, in this study, buckling of the curved beams is prevented by adding a penalty factor in the optimization program to avoid negative stiffness, see the details about the complete mathematical formula of the geometry optimization in Supporting Information.

So far, it has been proved that programmable QZS features can be achieved through our tailored mechanical metamaterials. Next, vibration tests are conducted to demonstrate that excellent vibration isolation effects in ultralow frequency ranges can be realized through the achieved QZS features. The experimental setup is shown in **Figure 4**a. One metamaterial sample characterized by the assembly matrix [1 1 1; 2 3 4] (see the left panel of Figure 4b) is installed on an electromechanical shaker (LDS V406 from Bruel & Kjaer VTS Ltd.). The support mass is appropriately adjusted and attached on the surface of the sample. Two identical accelerators (Type 4516 from Bruel & Kjaer VTS Ltd.) are attached on the bottom and top surfaces of the sample, serving to receive input and output signals, respectively. The white noise signal is generated by the signal generation module included in the dynamic signal collection system (PHOTON+ from Bruel & Kjaer VTS Ltd.), and then amplified by power amplifier (LDS LPA600 from Bruel & Kjaer VTS Ltd.). The acceleration signals are measured and acquired by the dynamic signal collection system.

The compression response of a metamaterial sample digitalized by the matrix [1 1 1; 2 3 4] is presented in the right panel of Figure 4b. Three plateaus respectively corresponding

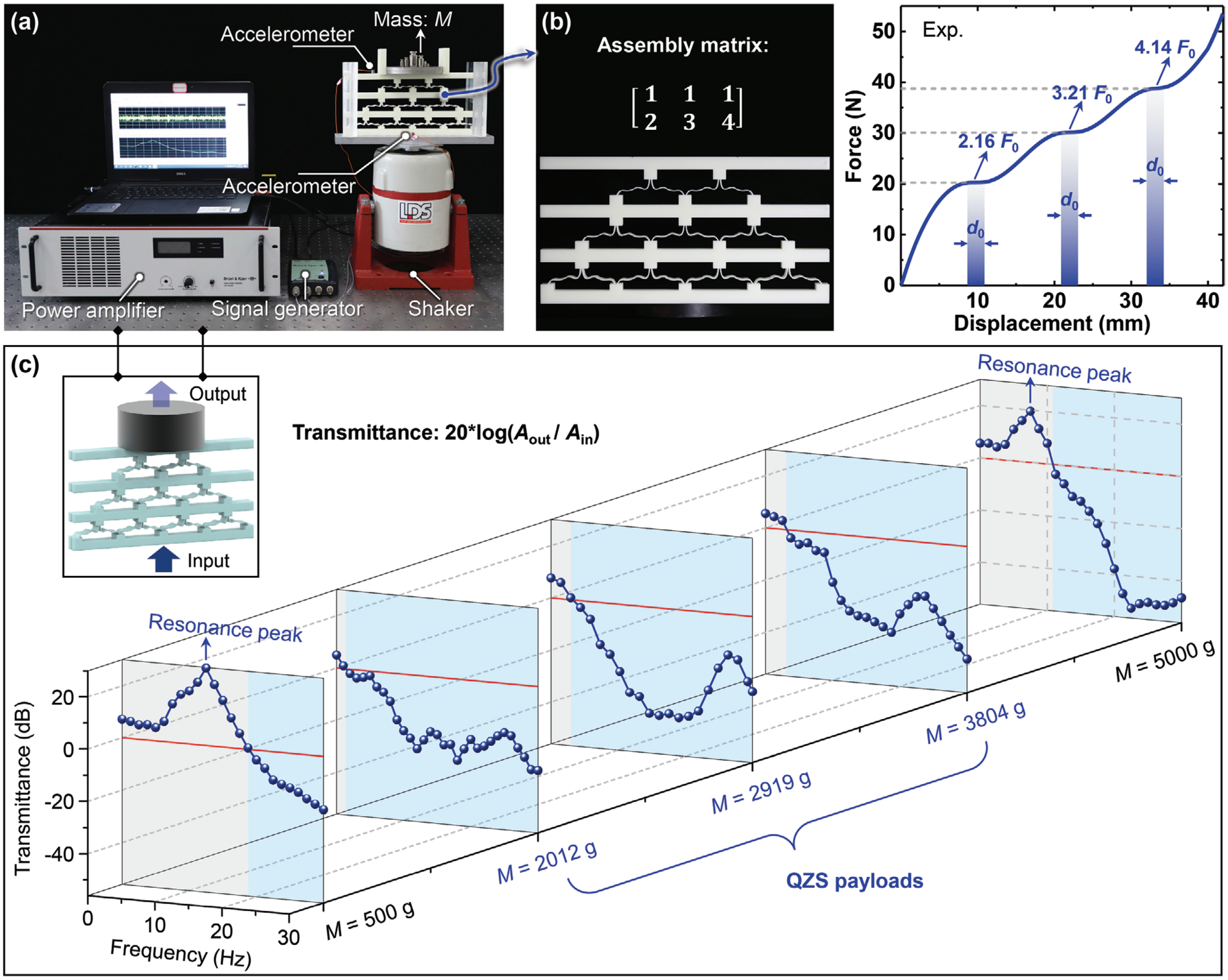

Figure 4. Experimental vibration tests. a) Instrument setup to measure the vertical vibration performance of the mechanical metamaterials. b) The sample used in the vibration tests is characterized by the assembly matrix [1 1 1; 2 3 4]. The right panel shows the experimentally measured force-displacement curve of a metamaterial sample characterized by this matrix. c) The experimentally measured transmittance curves under five typical support masses, with three among them corresponding to the QZS payloads.

to the QZS payloads 2.16*F_0, 3.21*F_0 and 4.14*F_0 are observed, where F_0 is the QZS payload of the printed single cell obtained from Figure 2e. The coefficients 2.16, 3.21, and 4.14 are close to the predicted values 2.0, 3.0, and 4.0, and the main reason for the existing difference is as follows. In the as-designed structure, all the curved beams have the same in-plane thickness of 1.0 mm. However, in the printed metamaterial samples, the in-plane thickness of the curved beams shows a certain deviation from 1.0 mm, with the maximum deviation reaching 8% in the measured data set, as shown by Figure S12, Supporting Information. Since the in-plane thickness of the printed single cell and that of the sample in Figure 4b (also the samples in Figure 3) are not completely the same, the obtained coefficients corresponding to the QZS payloads show certain deviations from the predicted integer values. To test the performance of the mechanical metamaterial in ultra-low frequency vibration isolation, the transmissions under different support masses are evaluated (see Figure 4a). The transmittance is defined by 20*log(A_{out}/A_{in}), where A_{out} is the amplitude of acceleration at the support mass and A_{in} is the amplitude of acceleration generated by the shaker. It should be noted that the sample shown in Figure 4a is not the one shown in Figure 4b. Considering place the support mass steadily on the top of the metamaterial, we printed a new sample shown in Figure 4a for the vibration tests. In this sample, a pair of auxiliary pillars is designed to ensure that the support mass is placed in the center of the top of the sample. The pair of pillars also restrains the support mass to prevent it from sliding and falling. Figure 4c shows the transmittances under five typical support masses, with three among them corresponding to the QZS payloads. So, how to determine the values of these three support masses? The QZS payloads (i.e., 2.16*F_0, 3.21*F_0, and 4.14*F_0) on the force–displacement curve shown in Figure 4b are selected as a reference. Taking the first QZS payload as an example, we first place the mass corresponding to $2.16*F_0$ on the top of the sample, and then record the transmission response of the system while adjusting the support mass by standard weights. When the system has low transmittance in the whole low frequency range, the support mass corresponding to the first QZS payload is determined. Similarly, we can determine the other two support masses corresponding to the second and third QZS payloads of the sample in Figure 4a. The results experimentally show that the mechanical metamaterial can significantly shield vibrations over almost the entire low frequency range when the support mass corresponds to the QZS payload. In comparison, for cases with other support masses ($M = 500$ g and $M = 5000$ g), resonance peak with high transmittance is observed in the studied low frequency range (0–30 Hz).

3. Conclusion

In summary, we have proposed a novel strategy to construct a type of compliant mechanical metamaterial with greatly enhanced programmability on overall mechanical behavior, such as the force–displacement curve and the quasi-zero-stiffness (QZS) feature. These are demonstrated by the combination of experiments, NURBS-based design optimization, and FEM simulations. This concept can be used to design and fabricate versatile metamaterials or metastructures with multiple QZS working ranges, which enables ultra-low frequency vibration isolation without sacrificing the loading capacity. Additionally, the proposed programming strategy can also offer new insights for the design of compliant mechanisms, which typically require achieving a customized force–displacement curve through rational geometry design optimization.

Supporting Information

Supporting Information is available from the Wiley Online Library or from the author.

Acknowledgements

The authors thank the National Natural Science Foundation of China (Grants No. 11632003, No. 11972083, No. 11991030, No. 11991033, and No. 12002030) and the Postdoctoral Innovation Talents Support Program (Grants No. BX20200052). The authors thank Prof. Kai Zhang and Yiwen Li for assisting the experiments and graphical illustration.

Conflict of Interest

The authors declare no conflict of interest.

Data Availability Statement

The data that support the findings of this study are available from the corresponding author upon reasonable request.

Keywords

mechanical metamaterial, programmability, quasi-zero stiffness, vibration isolation

Received: February 10, 2021
Revised: April 28, 2021
Published online:

[1] C. M. Harris, A. G. Piersol, *Harris' Shock and Vibration Handbook*, McGraw-Hill, New York **2002**.
[2] P. M. Alabuzhev, *Vibration Protection and Measuring Systems with Quasi-Zero Stiffness*, CRC Press **1989**.
[3] R. A. Ibrahim, *J. Sound Vib.* **2008**, *314*, 371.
[4] L. Wu, Y. Wang, Z. Zhai, Y. Yang, D. Krishnaraju, J. Lu, F. Wu, Q. Wang, H. Jiang, *Appl. Mater. Today* **2020**, *20*, 100671.
[5] Q. Cao, M. Wiercigroch, E. E. Pavlovskaia, C. Grebogi, J. M. T. Thompson, *Phys. Rev. E* **2006**, *74*, 046218.
[6] A. Carrella, M. J. Brennan, T. P. Waters, *J. Sound Vib.* **2007**, *301*, 678.
[7] X. Liu, X. Huang, H. Hua, *J. Sound Vib.* **2013**, *332*, 3359.
[8] C. Cai, J. Zhou, L. Wu, K. Wang, D. Xu, H. Ouyang, *Compos. Struct.* **2020**, *236*, 111862.
[9] D. Xu, Q. Yu, J. Zhou, S. R. Bishop, *J. Sound Vib.* **2013**, *332*, 3377.
[10] L. L. Howell, *Compliant Mechanisms*, Springer, New York **2013**.
[11] B. Haghpanah, L. Salari-Sharif, P. Pourrajab, J. B. Hopkins, L. Valdevit, *Adv. Mater.* **2016**, *28*, 7915.
[12] L. A. Shaw, S. Chizari, M. Dotson, Y. Song, J. B. Hopkins, *Nat. Commun.* **2018**, *9*, 4594.
[13] C. Coulais, A. Sabbadini, F. Vink, M. van Hecke, *Nature* **2018**, *561*, 512.
[14] L. Jin, A. E. Forte, B. Deng, A. Rafsanjani, K. Bertoldi, *Adv. Mater.* **2020**, *32*, 2001863.
[15] B. Florijn, C. Coulais, M. van Hecke, *Phys. Rev. Lett.* **2014**, *113*, 175503.
[16] C. Coulais, D. Sounas, A. Alù, *Nature* **2017**, *542*, 461.
[17] C. Luo, Y. Song, C. Zhao, S. Thirumalai, I. Ladner, M. A. Cullinan, J. B. Hopkins, *Mater. Horiz.* **2020**, *7*, 229.
[18] Q. Ma, H. Cheng, K.-I. Jang, H. Luan, K.-C. Hwang, J. A. Rogers, Y. Huang, Y. Zhang, *J. Mech. Phys. Solids* **2016**, *90*, 179.
[19] H. Zhang, X. Guo, J. Wu, D. Fang, Y. Zhang, *Sci. Adv.* **2018**, *4*, eaar8535.
[20] D. Yan, J. Chang, H. Zhang, J. Liu, H. Song, Z. Xue, F. Zhang, Y. Zhang, *Nat. Commun.* **2020**, *11*, 1180.
[21] O. R. Bilal, A. Foehr, C. Daraio, *Proc. Natl. Acad. Sci. USA* **2017**, *114*, 4603.
[22] B. Deng, S. Yu, A. E. Forte, V. Tournat, K. Bertoldi, *Proc. Natl. Acad. Sci. USA* **2020**, *117*, 31002.
[23] M. Hippler, K. Weißenbruch, K. Richler, E. D. Lemma, M. Nakahata, B. Richter, C. Barner-Kowollik, Y. Takashima, A. Harada, E. Blasco, M. Wegener, M. Tanaka, M. Bastmeyer, *Sci. Adv.* **2020**, *6*, eabc2648.
[24] T. Chen, M. Pauly, P. M. Reis, *Nature* **2021**, *589*, 386.
[25] S. Shan, S. H. Kang, J. R. Raney, P. Wang, L. Fang, F. Candido, J. A. Lewis, K. Bertoldi, *Adv. Mater.* **2015**, *27*, 4296.
[26] T. Frenzel, C. Findeisen, M. Kadic, P. Gumbsch, M. Wegener, *Adv. Mater.* **2016**, *28*, 5865.
[27] F. Pan, Y. Li, Z. Li, J. Yang, B. Liu, Y. Chen, *Adv. Mater.* **2019**, *31*, 1900548.
[28] K. Fu, Z. Zhao, L. Jin, *Adv. Funct. Mater.* **2019**, *29*, 1901258.
[29] K. Yu, N. X. Fang, G. Huang, Q. Wang, *Adv. Mater.* **2018**, *30*, 1706348.
[30] L. Jin, R. Khajehtourian, J. Mueller, A. Rafsanjani, V. Tournat, K. Bertoldi, D. M. Kochmann, *Proc. Natl. Acad. Sci. USA* **2020**, *117*, 2319.

[31] Y. Chen, X. Li, G. Hu, M. R. Haberman, G. Huang, *Nat. Commun.* **2020**, *11*, 3681.
[32] X. Li, Y. Chen, X. Zhang, G. Huang, *Extreme Mech. Lett.* **2020**, *39*, 100837.
[33] O. R. Bilal, A. Foehr, C. Daraio, *Adv. Mater.* **2017**, *29*, 1700628.
[34] Z. Wang, Q. Zhang, K. Zhang, G. Hu, *Adv. Mater.* **2016**, *28*, 9857.
[35] H. Liu, Q. Zhang, K. Zhang, G. Hu, H. Duan, *Adv. Sci.* **2019**, *6*, 1900401.
[36] Y. Zhang, B. Li, Q. S. Zheng, G. M. Genin, C. Q. Chen, *Nat. Commun.* **2019**, *10*, 5605.
[37] C. V. Jutte, S. Kota, *J. Mech. Design* **2008**, *130*, 081403.
[38] P. Wang, Q. Xu, *Mech. Mach. Theory* **2018**, *119*, 1.
[39] J. Zhou, H. Pan, C. Cai, D. Xu, *Int. J. Mech. Mater. Des.* **2020**, 1.
[40] K. Che, C. Yuan, J. Wu, H. Jerry Qi, J. Meaud, *J. Appl. Mech.-T. ASME* **2017**, *84*, 011004.
[41] H. Yang, L. Ma, *J. Mater. Sci.* **2019**, *54*, 3509.
[42] T. J. Hughes, J. A. Cottrell, Y. Bazilevs, *Comput. Methods Appl. Mech. Engrg.* **2005**, *194*, 4135.
[43] X. Zhang, J. Yao, B. Liu, J. Yan, L. Lu, Y. Li, H. Gao, X. Li, *Nano Lett.* **2018**, *18*, 4247.
[44] S. Yuan, C. K. Chua, K. Zhou, *Adv. Mater. Technol.* **2019**, *4*, 1800419.